Soft Matter

Microswimmers under the spotlight: interplay between agents with different levels of activity

Journal:	*Soft Matter*
Manuscript ID	SM-ART-07-2023-000915.R1
Article Type:	Paper
Date Submitted by the Author:	28-Aug-2023
Complete List of Authors:	Desgranges, Caroline; University of Massachusetts Lowell, Physics and Applied Physics Ferrari, Melissa; New York University, Department of Physics Chaikin, Paul; New York University, Department of Physics Sacanna, Stefano; New York University, Chemistry Tuckerman, Mark; New York University, Department of Chemistry and Courant Institute of Mathematical Sciences Delhommelle, Jerome; University of Massachusetts Lowell, Department of Chemistry

Soft Matter

ARTICLE TYPE

Cite this: DOI: 00.0000/xxxxxxxxxx

Microswimmers under the spotlight: interplay between agents with different levels of activity

Caroline Desgranges,[a] Melissa Ferrari,[b] Paul M. Chaikin,*[b] Stefano Sacanna,[c] Mark E. Tuckerman,[b,c,d,e,f] and Jerome Delhommelle,*[g]

Received Date
Accepted Date

DOI: 00.0000/xxxxxxxxxx

The ability of active matter to assemble into reconfigurable nonequilibrium structures has drawn considerable interest in recent years. We have investigated how active fluids respond to spatial light patterns through simulations and experiments on light-activated self-propelled colloidal particles. This work delves into the processes of inverse templated assembly, which involves creating a region without active particles through a bright pattern, and templated assembly, which promotes the formation of dense particle regions through a dark pattern. We identify scaling relations for the characteristic times for both processes that quantify the interplay between the dimension of the applied pattern and the intrinsic properties of the active fluid. We also explore the assembly mechanism and dynamics of large clusters and examine how assembly and inverse assembly can be combined to create any arbitrarily complex template. In addition to providing protocols for templated assembly via light patterning, our results show how the local packing fraction can be fine-tuned by modulation of the light intensity. This exceeds the capabilities of conventional assembly strategies, in which packing fraction is dictated by thermodynamics, and opens the door to arbitrarily precise and programmable nonequilibrium assembly strategies in active matter.

1 Introduction

Active matter exhibits a wealth of behaviors that arise from its nonequilibrium nature[1–13]. Indeed, even "simple" active fluids, *i.e.*, purely repulsive self-propelled particles or active Brownian particles (ABPs), exhibit a motility-induced phase transition (MIPS)[14–16] akin to a liquid-vapor transition, even in the absence of any attractive interparticle interactions[17–23]. The constant influx of chemical energy into the system drives motility and breaks time-reversal symmetry and detailed balance, leading to the emergence of these unique features[24]. Another unique property of active particles is the relation that exists between the steady-state particle density ρ and the local self-propulsion velocity v_0, with active particles accumulating in regions where v_0 is low[25]. This provides a novel avenue for promoting self-assembly through the spatial control of activity[26,27]. This strategy has been successfully leveraged to trigger the assembly of synthetic self-propelled particles, for which the application of a specific light pattern can, for instance, allow for the programmable, light-induced, self-assembly of active rectification devices[26]. A similar strategy has also been employed for biological systems[28–30] since, under anaerobic conditions, *E. coli* bacteria can express proteorhodopsin, a green-photon-driven proton pump[31,32]. Templated active self-assembly can thus be achieved for living systems using light-controlled bacteria[28–30].

To achieve the promise of a smart, programmable, templated self-assembly, we need to identify the key parameters and determine the equations that govern the dynamics of the assembly process. This requires a quantification of the response of the active fluid to a real-time reconfiguration of the light field. In previous work, Arlt *et al.*[28,29] considered an active suspension of *E. coli* bacteria uniformly illuminated, *i.e.*, moving at a (constant) saturation self-propulsion velocity v_0. They subjected the system to a light pattern consisting of a bright $L_0 \times L_0$ square against a dark background, with L_0 being of the same order as the persistence length L_p of the bacteria, and reported that the time τ necessary to empty the square obeys the following scaling relation $\tau \sim L_0/v_0$. In addition, they found diffusive dynamics for the peak

[a] Department of Physics & Applied Physics, University of Massachusetts, Lowell, MA 01854, USA.
[b] Department of Physics, New York University, 726 Broadway, New York, New York 10003, USA. Tel: (212) 998-7694; E-mail: chaikin@nyu.edu
[c] Department of Chemistry, New York University (NYU), New York, New York 10003, USA.
[d] Courant Institute of Mathematical Sciences, New York University (NYU), New York, New York 10012, USA.
[e] NYU-ECNU Center for Computational Chemistry at NYU Shanghai, 3663 Zhongshan Road North, Shanghai 200062, China.
[f] Simons Center for Computational Physical Chemistry at New York University, New York, New York 10003, USA.
[g] Department of Chemistry, University of Massachusetts, Lowell, MA 01854, USA. Tel: (978) 934-4367; E-mail: jerome_delhommelle@uml.edu

of maximum bacterial density in dark regions, noting that quantitative aspects remained to be elucidated[28]. The objective of this work is to use simulations on active Brownian particles[33,34] and experiments on synthetic, light-activated, self-propelled particles[2,35] to extend Artl *et al.*'s work to a broad range of ratios of L_0 (a characteristic length scale for the system) to L_p (the persistence length of the swimmers) and obtain a quantitative characterization of light-templated assembly processes in active fluids. Our goal is three-fold: (i) to obtain scaling relations for the characteristic times of inverse templated assembly and templated assembly, (ii) to analyze the mechanism and dynamics of the onset of templated assembly at the particle level, and (iii) to identify a protocol for programmable and modulated templated assembly. By varying the activity level of the particles, we can achieve precise control through arbitrarily complex light patterns.

The paper is organized as follows. In the upcoming section, we will introduce the simulation models and methods we utilize to examine 2D active systems composed of self-propelled repulsive disks. Additionally, we will discuss how we define and apply spatial light patterns to control assembly alongside the corresponding experiments. We will then present the results obtained for the time dependence for inverse templated assembly and templated assembly. In both cases, we will identify the scaling of the characteristic time for the process with the pattern size and the active fluid parameters, and we will analyze the microscopic mechanisms and dynamics of templated assembly for clusters of increasing size. We will combine patterns for the two types of processes to form an overall pattern with a checkerboard motif that we apply to active matter in experiments and simulations. The results demonstrate the ability of this stimulus-controlled nonequilibrium assembly to precisely fine-tune the local packing fraction according to a programmed light pattern. This exceeds the capability of many passive assembly processes for which thermodynamics controls the local density. Finally, we will summarize the key conclusions from this work in the last section.

2 Methods and models

2.1 Simulations

We carry out simulations on systems of two-dimensional active particle systems defined as disks of radius a. The packing fraction of the system is given by $\phi = \frac{N\pi a^2}{L^2}$, where L is the length of the simulation cell. Each colloidal disk[33,34,36] is described by the position $\mathbf{r}_i$ of its center and the orientation θ_i of a polar axis $\hat{\mathbf{n}}_i = (\cos\theta_i, \sin\theta_i)$. Two disks i and j interact through:

$$\Phi(r_{ij}) = \begin{cases} \frac{k}{2}(2a - r_{ij})^2 & r_{ij} < 2a \\ 0 & r_{ij} \geq 2a \end{cases} \quad (1)$$

in which r_{ij} denotes the distance between the disks i and j, and k is a force constant.

The equations of motion are given by

$$\begin{aligned} \partial_t \mathbf{r}_i &= s(\mathbf{r}) v_0 \hat{\mathbf{n}}_i + \mu \textstyle\sum_{j\neq i} \mathbf{F}_{ij} + \sqrt{2D_T}\,\eta_i^T \\ \partial_t \theta_i &= \sqrt{2D_R}\,\eta_i^R \end{aligned} \quad (2)$$

where v_0 is the single-particle self-propulsion speed, $\mathbf{F}_{ij} = -\vec{\nabla}_i \Phi(r_{ij})$ is the force exerted on i through the interaction between i and j, $\mu = \frac{D_T}{k_B T}$ the mobility, and D_T and D_R are the translational and rotational diffusion constants. The function $s(\mathbf{r})$ is a control parameter that quantifies the light intensity ($0 \leq s(\mathbf{r}) \leq 1$) in the region where the particle is located. The η_i are Gaussian white noise processes having zero mean and correlation $\langle \eta_i(t)\eta_j(t')\rangle = \delta_{ij}\delta(t-t')$. In our model, we explicitly include the term corresponding to translational diffusion in the equations of motion. This differs from Fily *et al.*'s model, which was developed for active systems subjected to uniform and constant lighting. In their case, the effect of translational diffusion was negligible when compared to the self-propulsion term[33,34]. Here, since we examine the dynamics of particles in regions without any illumination and where the particles become passive, we need to account for the translational diffusion term in the equations of motion in addition to the rotational diffusion.

In this study, we expose self-propelled particles to a light pattern that includes either a bright ($s(\mathbf{r}) > 0$) or a dark ($s(\mathbf{r}) = 0$) region with a characteristic size of L_0. The examples analyzed in this work use L_0 as the edge of a square or the width of a strip. The parameter space includes five variables: packing fraction ϕ, translational diffusion constant D_T, rotational diffusion constant D_R, self-propulsion velocity v_0, and L_0. To reduce the number of variables, we can use the relation $D_R = \frac{3D_T}{4a^2}$ for spheres in the low-Reynolds number regime[37] and the fact that the particles undergo a random walk with a persistence length $L_p = \frac{D_R}{v_0}$. This leaves us with three variables to explore: ϕ, L_p, and v_0 while keeping D_R and L_0 constant.

Throughout this work, we use a reduced system of units with the particle radius a as the unit of length and $(\mu k)^{-1}$ as the unit of time to make the equations of motion, simulation parameters, and results dimensionless. The equations of motion are integrated using the Euler method with a time step of $\tau = 5\times10^{-4}$ in reduced units. The rotational and translational diffusion constants are set to $D_R = 5\times10^{-4}$ and $D_T = 6.7\times10^{-4}$, the cutoff for the interactions to $r_c = 2$ and the usual periodic boundary conditions are applied[38]. We carry out simulations for 2D systems with $N = 10000$ particles. We vary the packing fraction from $\phi = 0.05$ to 0.2, the self-propulsion velocity from $v_0 = 5\times10^{-3}$ to 1 and the characteristic dimension of the light pattern from $L_0 = 25$ to 300. This corresponds to Péclet numbers $P_e = v_0 a/D_T$ ranging from ~ 7.5 to ~ 1500, to persistence lengths L_p ranging from 10 and 2000, and to $\frac{L_0}{L_p}$ ratios between ~ 0.01 and 20. These conditions allow us to study the impact of packing fraction on light-directed assembly in the absence of any spontaneous formation of clusters via MIPS ($\phi \sim 0.4$ and above) [34].

We analyze the number fluctuations[33] $\langle(\Delta N)^2\rangle = \langle N^2\rangle - \langle N\rangle^2$ to detect the formation of inhomogeneity and the onset of MIPS[17–23], marked by a bimodal distribution of local densities as shown by Redner *et al.*[37]. To perform this analysis, we divide the system into subsystems (squares) with a given edge and calculate the fluctuations in the number of particles N_s within this square size. By varying the square size, we obtain the size dependence of $\langle(\Delta N)^2\rangle$ and show the simulation results obtained for v_0 ranging from 5×10^{-3} to 1 in Fig. 1. We observe that the results fall roughly onto the same plot and fit the data to $\langle(\Delta N)^2\rangle \sim N_s^{\beta}$, where β is a fitting parameter. We recall that $\beta = 1$ indicates a

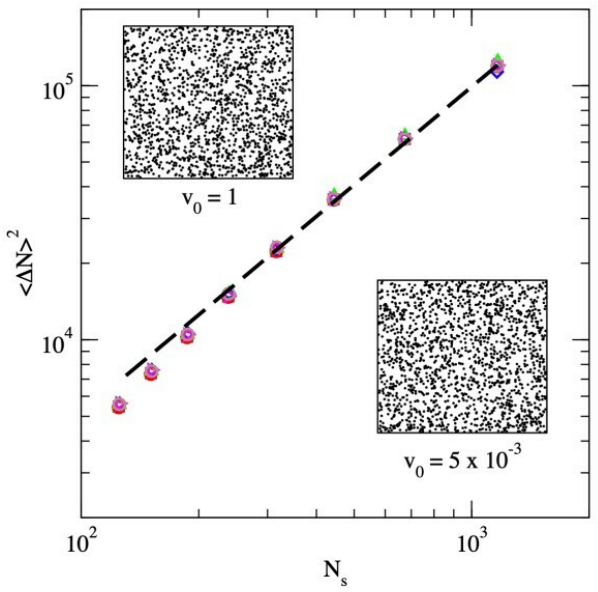

Fig. 1 Number fluctuations for $\phi = 0.2$ and varying values of v_0 ranging from 5×10^{-3} to 1 plotted as symbols. Results for all velocities fall onto the same line, which has been fitted to a power law N_s^{β} with $\beta = 1.28$. The inset displays snapshots of the system configurations for $v_0 = 1$ (top left) and $v_0 = 5 \times 10^{-3}$ (bottom right), which confirm the absence of any phase separation or onset of MIPS in the system.

homogeneous system, while $\beta = 2$ corresponds to a phase separation and the onset of MIPS. The plot shown as a dashed line in Fig. 1 corresponds to a value of $\beta = 1.28$ that is much closer to the value of 1 expected for a homogeneous system than to the value of 2 expected for a phase-separated system undergoing MIPS. Indeed, Fily *et al.* set a limit of $\beta > 1.5$ as the threshold for the onset of MIPS[34]. Our results thus confirm that no spontaneous cluster formation is observed under uniform illumination for the (v_0, ϕ) sets of conditions examined in this work and that any assembly observed in this work is due to the application of a light pattern. While the absence of clustering and MIPS in the simulations is due to the low packing fraction of the system, the Péclet number can also serve as a control parameter for the onset of MIPS. In the experiments, we prevent MIPS by setting the Péclet number. More specifically, by fine-tuning the intensity of light, we achieve low enough Péclet numbers to avoid clustering and MIPS.

2.2 Experiments

In this section, we detail the procedures and implements necessary for fabricating, imaging, and manipulating our colloidal swimmers.

Particle Fabrication. The bimaterial colloidal particles were prepared in the Sacanna Lab following the same protocol outlined in reference[2].

Sample Preparation. The swimmers fabricated in the last section can only swim if immersed in an appropriate solution of dilute hydrogen peroxide. Two main protocols for solution preparation are used in this work. The first was outlined in [2] and the second, was developed to increase the propulsive speed of the particles.

1. Swimmers are dispersed in a basic solution with pH $\sim$ 8 containing 5mM tetramethylammonium hydroxide (TMAH) and 3%w=w hydrogen peroxide (H_2O_2).

2. Swimmers are dispersed in a buffer solution containing 2mm Bis-Tris and 3%w=w hydrogen peroxide (H_2O_2).

Sample Cell Preparation. The solution of swimmers prepared in the previous section is either loaded into a commercially available or a custom-made sample cell for imaging. The design, composition, and cleanliness of the sample cell will dictate the swimmer-surface interaction, the imaging conditions, and the maximal length of a single experimental study. The particles have a density $\rho_{swimmer} = 1.55 g/cm^3$ which is much greater than that of water ($\rho_{water} = 1 g/cm^3$) causing them to settle due to gravity at the bottom of the sample cell. With the particles in close contact with a sample cell's surface, there is a potential for strong interaction with the substrate and steps must be taken to prevent any undesirable interaction. Details can be found in the Electronic Supplementary Information.

Digital Video Microscopy. We utilize digital video microscopy to image swimming activity and track the individual trajectories of colloidal swimmers. To image the sample, we secure it onto the sample stage of an inverted microscope (Nikon Ti-U) that is equipped with a brightfield illumination source (LIDA LED Illuminator). The red LED is typically used as the illumination source to ensure the imaging light does not activate the propulsive mechanism of the swimmers. The image of the illuminated sample is magnified by an objective lens (Nikon Plan Fluor, 10×, N.A. 0.30; Nikon Plan Apo Lambda 20×, N.A. 0.75; Nikon Plan Apo Lambda 40×, N.A. 0.95) before being relayed to the imaging plane of a digital camera (Imaging Source DFK33UX174). The camera records at a frame rate of 1-30 frames per second with a resolution of 1920×1200 pixels. The resulting field of view for each of the objective lenses listed above spans approximately $703 \times 1125 \mu m$ (for 10×), $352 \times 564 \mu m$ (for 20×), and $178 \times 284 \mu m$ (for 40×). To activate the swimmers, the sample is typically illuminated by a light engine (SOLA-SE2) with a high-pass filter (Semrock FF506). A removable low-pass filter (Edmund 47-287) is placed before the camera to block illumination from the activating light engine and improve imaging quality.

Structured Illumination Setup. The modification and integration of a commercially available and inexpensive projector has been used for constructing spatial light patterns. This method has been also adapted in a range of experiments including imaging and tracking larvae on the sub-millimeter scale as well as photolithography on the sub-micrometer scale.

Projecting Images into the Focal Plane of a Microscope. Commercial projectors are designed to form and magnify digital images at some distance in the foreground. A light source illuminates a digital mirror array and the image defined at the digital mirror object plane is relayed through a divergent lens, forming an enlarged projected image. Through the removal of the diverging lens in the projector's optical path and incorporation of a customized relaying lens setup at the object plane of the digital micromirror device (DMD), one can configure the optical path to relay the image through the optical train of an inverted

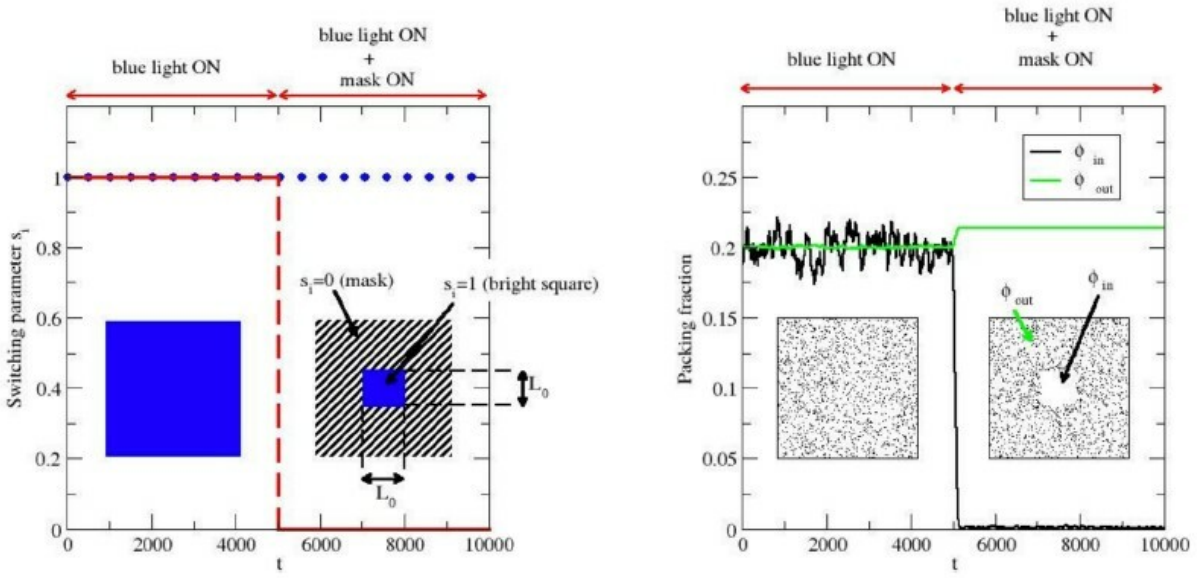

Fig. 2 (Left panel) Light pattern for inverse templated assembly. The entire system is illuminated for $0 \leq t \leq 5000$ (left inset). For $t > 5000$, the light is kept shining in a central square of edge L_0 and switched off everywhere else (right inset). The control parameter $s(\mathbf{r})$ is shown as a function of time as filled blue circles for the central region and as a red dashed line for the surroundings. (Right panel) Packing fraction ϕ for the central region (black line) and the surroundings (green line). The left inset shows a snapshot at $t = 5000$, revealing a uniform particle distribution. The right inset shows a snapshot at $t = 10000$, with an empty central region, $L_0 \times L_0$, as particles have moved to the surroundings.

microscope, through an objective lens, and onto the focal plane containing a sample with scale dictated by the customizable optical components.

Integrating the Projector. An illumination pattern is defined as a two-dimensional array of 8-bit integers and is sent to the projector through an HDMI cable; each mirror in the DMD will toggle with a frequency proportional to the integer values of the illumination pattern. The image is embedded in the external illumination as it reflects off the DMD. The image then passes through an optical relay where it is demagnified and sent to the focal plane of the microscope objective. The projector is controlled using its commercially available graphical user interface (GUI). Patterns are first created with a commercial presentation program and sent to the projector through an HDMI cable.

3 Results and Discussion

3.1 Templated Inverse Assembly and Templated Assembly via Light Patterns

We start by examining the mechanism and kinetics of light-templated inverse assembly. To simulate the templated inverse assembly process and identify scaling relations for its characteristic time, We apply a light pattern that promotes the creation of an empty space in the shape of a square, without any particles present[26,28]. To achieve this in our simulations, we illuminate the square region to create a bright pattern and keep the surrounding areas dark, as simulated in Figure 2(a).

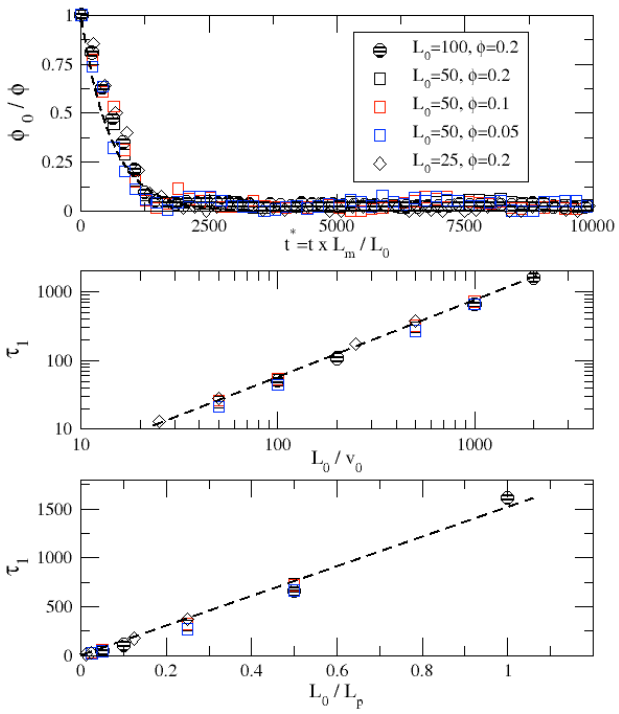

Fig. 3 Inverse templated assembly. Here the control parameter $s(r) = 1$ or 0. (Top) Scaled packing fraction ϕ_0/ϕ in the bright square against the scaled time (the scaling factor $L_m = 100$ denotes the maximum size used for the square in this work, and the origin $t^* = 0$ corresponds to the activation of the light pattern), with the exponential fit of Eq. 3 shown as a dashed line. (Middle) Characteristic time τ_1 for the inverse assembly process against L_0/v_0, with a linear fit (dashed line). (Bottom) Characteristic time τ_1 against L_0/L_p, together with a linear fit with slope 1 (dashed line).

The impact on the system is shown in Fig. 2(b), where we plot the variation of the packing fraction in the bright and dark regions. The initially uniform active fluid, shown in the left inset, quickly rearranges into a system with two regions of different densities. There is a sharp decrease in the packing fraction for the central region at a location that matches the bright pattern and a sharp increase in the packing fraction everywhere else where the light has been turned off (see also Movie 1 provided in the Electronic Supplementary Information).

In Fig. 3, we present the time-dependent packing fraction in the central region, denoted as ϕ_0, for various square sizes L_0 and overall packing fractions ϕ, with a fixed self-propulsion velocity of $v_0 = 0.1$. After scaling ϕ_0 by ϕ and adjusting time using the formula $t^* = t \times L_m/L_0$ (where $L_m = 100$ and corresponds to the maximum size used for the square in this work), we observe that ϕ_0/ϕ results for different square sizes follow the same pattern. This finding is consistent with the experimental results of Artl *et al.*[28]. We also demonstrate that this behavior holds for various packing fractions in the $0.05 < \phi < 0.2$ range. By fitting the simulation results to an exponential function, we can extract the relaxation time

$$\frac{\phi_0}{\phi} = \exp\left(-\frac{t^*}{\tau_1}\right) \tag{3}$$

and report the variation of τ in the top plot of Fig. 3.

First, we plot τ_1 against the L_0/v_0 ratio. This ratio represents the time required for particles traveling at v_0 to traverse a distance of L_0, enabling them to exit the illuminated square area. The linear graph in the middle of Fig. 3 confirms the expected proportionality of $\tau_1 \sim (L_0/v_0)$. Additionally, we generate a plot of τ_1 versus L_0/L_p, where L_p denotes the persistence length, to establish a broader statement about this linear relationship. Our results demonstrate that $\tau_1 \sim L_0/L_p$ within the $0.01 < L_0/L_p < 1$ range. These findings extend the conclusions drawn by Artl *et al.*[28] to encompass a wider range of L_0/L_p ratios within systems that have an *E. coli* persistence length comparable to the pattern size.

The next step involves reversing the light pattern to achieve a templated assembly and identifying the scaling relations for its characteristic time. This can be accomplished by using a light pattern with a central dark region and illuminated surroundings, as demonstrated by our simulations (refer to the inset of Fig.4). The simulations exhibit the formation of square clusters of particles when such a light pattern is applied (also visible in Movie 2, provided in the Supplementary Information). Our focus now is on determining the scaling relation for the formation time of this cluster and analyzing the time dependence of the packing fraction in the dark region. We denote the increase in packing fraction ϕ_0 compared to the initial (uniform) packing fraction ϕ as $\Delta\phi = \phi_0 - \phi$. We define τ_2 as the characteristic time to fill the square. Thus, τ_2 is the time required for N_0 particles to reach the square, with $N_0 \sim \phi_{max} L_0^2$ where ϕ_{max} is the maximum packing fraction (assumed to be equal to 1 for simplicity in the derivation of the scaling relation). The N_0 particles are taken from the illuminated surroundings and therefore are confined within a square of area $\sim (\tau_2 v_0)^2$ of packing fraction ϕ, resulting in $N_0 \sim \phi(\tau_2 v_0)^2$.

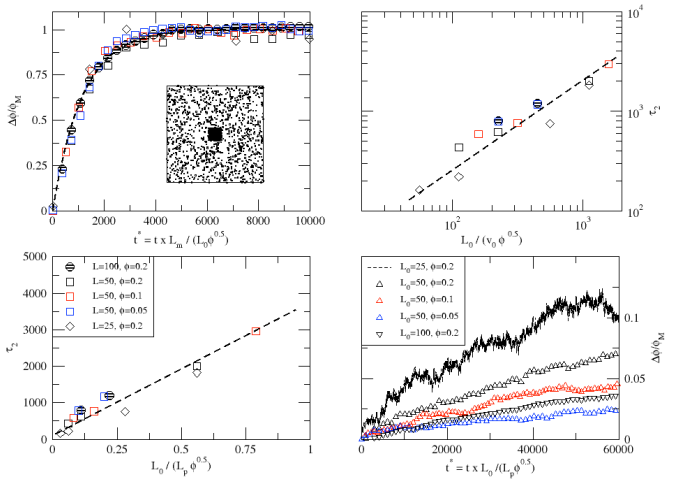

Fig. 4 Templated assembly. (Top left) Scaled packing fraction $\Delta\phi/\Delta\phi_M$ in the dark square against scaled time at $v_0 = 0.1$ and $\phi = 0.2$ for $L_0 = 25$ (diamonds), $L_0 = 50$ (black squares) and $L_0 = 100$ (dashed circles). Results are also shown for $L_0 = 50$ at $v_0 = 0.1$ (red squares) and $\phi = 0.05$ and $\phi = 0.1$ (blue squares) (the scaling factor $L_m = 100$ denotes the maximum square size used in this work, and the origin $t^* = 0$ corresponds to the activation of the light pattern), with the exponential fit of Eq. 5 shown as a dashed line. (Top right) Characteristic time τ_2 for the assembly process against $L_0/(v_0\phi^{0.5})$ and linear fit (dashed line). (Bottom left) Characteristic time τ_2 against $L_0/(L_p\phi^{0.5})$ and linear fit (dashed line). (Bottom right) Scaled packing fraction against the scaled time for $v_0 = 5 \times 10^{-3}$.

This leads to the following expected scaling behavior for τ_2.

$$\tau_2 \sim \frac{L_0}{\sqrt{\phi} v_0} \tag{4}$$

To plot the behavior of $\Delta\phi/\Delta\phi_M$ as a function of scaled time t^*, we scaled $\Delta\phi$ by its maximum value $\Delta\phi_M$ for each set of conditions and used the formula $t^* = t \times \frac{L_m}{L_0\sqrt{\phi}}$. The resulting graph, shown in Fig. 4, displays the system's behavior for a given velocity $v = 0.1$, with square sizes ranging from 25 to 100 and packing fractions between 0.05 and 0.2. All results fall onto the same plot, indicating a similar relaxation behavior that we fit with the following exponential functional form

$$\frac{\Delta\phi}{\Delta\phi_M} = \left(1 - \exp\left(-\frac{t}{\tau_2}\right)\right) \tag{5}$$

τ_2 is also shown as a function of $L_0/(v_0\sqrt{\phi})$ and of $L_0/(L_p\sqrt{\phi})$ in Fig. 4.

The two plots demonstrate a linear scaling of τ_2, which is in agreement with our expectations and Eq. 4. Similarly to the scaling derived for the emptying time obtained for light patterns consisting of a bright square, the scaling obtained for the filling time applies to pattern sizes of the order as the persistence length. In Fig. 4, we present the relaxation behavior for a self-propulsion velocity of $v_0 = 5 \times 10^{-3}$, which corresponds to L_0/L_p ratios ranging from 2.5 to 10 for pattern sizes of 25 and 100, respectively. Our results indicate that the scaling behavior observed for lower L_0/L_p ratios does not apply to this regime, and we will examine the assembly dynamics for large patterns in the next section.

3.2 Assembly Mechanism and Dynamics for Large Patterns

We now turn to the dynamics of the assembly process when the system is subjected to a dark pattern that is significantly larger than the persistence length of the active fluid. To this end, we consider a rectangular simulation cell, elongated along the x axis such that $L_x = 25 \times L_y = 2000$ and simulate a system with $N = 10^4$ particles and number density $n = 0.063$. The pattern we apply in this case is a dark strip of fixed width along the x axis, with width $L_0 = 200$. We test a range of self-propulsion velocities from 10^{-1} to 1. In Figure 5, we provide snapshots of the system at regular intervals, with $v_0 = 1$ and a light pattern containing a dark strip of width $L_0 = 200$ at the center of $x = 0$.

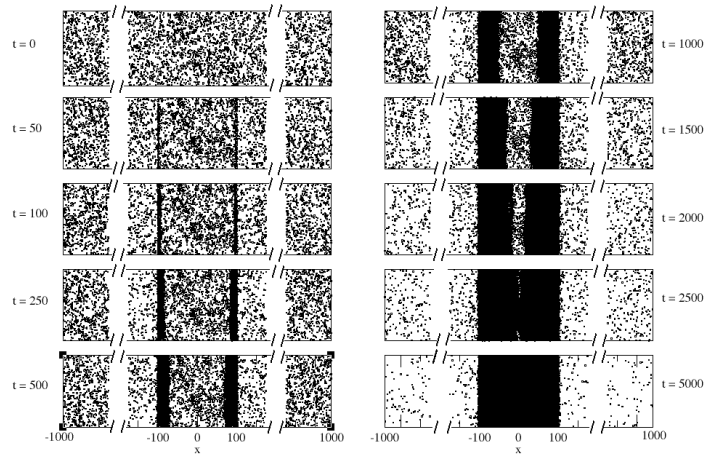

Fig. 5 Time evolution of a simulated active fluid ($v_0 = 1$) subjected to a light pattern with a central dark strip ($L_0 = 200$). The initial configuration is obtained by subjecting the system to uniform lighting. For $t > 0$, the only region illuminated is from -1000 to -100 and from 100 to 1000.

The snapshots provide insight into the assembly mechanism (see also Movie 3 provided in the Supplementary Information). Once the light is turned off, a dense zone quickly forms at the boundary between the dark and bright areas (see snapshot for time $t = 50$). This zone expands into the dark region as particles move from the illuminated region into the dark region through the boundary. Eventually, a front of particles emerges and gradually moves towards the center of the strip until both fronts merge at around time $t \sim 2500$.

We have gathered data to measure the assembly dynamics, presented in Fig. 6. The data includes particle density profiles at regular intervals, selected particle densities for specific x values, and the displacement of the front $\Delta x(t) = x(t) - x(0)$. The starting point of the front, $x(0)$, is at ± 100 for a strip of width $L_0 = 200$. The density profile shows a maximum at the boundary between the dark and bright regions. The density then decreases linearly with x between the boundary and the front, with the front moving closer to the center of the strip over time. Once the two fronts have merged, the density profile becomes flat between the two boundaries, indicating a quasi-uniform density across the strip. The number densities n_x measured for specific x values show that the density at the boundary ($x = 100$) increases rapidly to the maximum number density for the system before reaching a plateau. The number densities inside the strip ($0 \leq x < 100$) gradually increase with time and converge towards roughly the same value for a long time. Conversely, the number density outside the dark strip, n_{150}, decreases from its initial value $n_{150}(0) = \phi/\pi$ with time as particles leave the bright region to enter the dark strip. We also examine the time-dependence of the front $\Delta x(t)$ (see the bottom plot of Fig. 6) and find, for large t. This asymptotic behavior is consistent with a diffusive behavior, as shown by the linear fit to a $t^{0.5}$ functional form, in line with the experimental findings of Artl *et al.*[28]. We add that, for short times, the front moves at a much faster pace, as particles, which are active with a self-propulsion velocity of v_0 in the bright region, are thrust into the dark strip close to the boundary and only start to be simply passive (diffusive) particles further inside the strip.

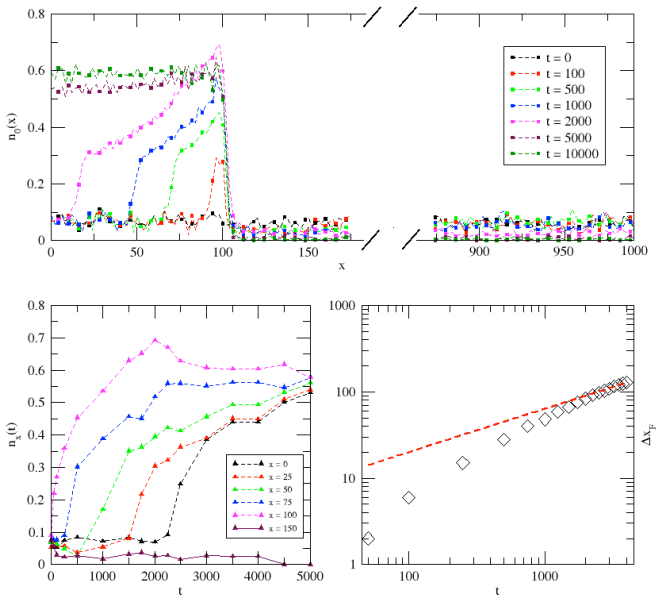

Fig. 6 (Top) Profile for the number density across the positive half of the strip with the boundary between the dark and bright regions at $x = 100$ (same system as in Fig. 5). (Bottom left) Time dependence of the number density $n_x(t)$ at selected x values across the strip. (Bottom right) Front position Δx as a function of time. The dashed line corresponds to a fit to a $t^{0.5}$ function form for large times.

3.3 Smart Templated Active Self-Assembly with Complex Light Patterns

We generalize this approach to the templated assembly of larger ($L_0 \geq 10 L_p$) and more complex patterns. To this end, we carry out experiments and simulations of active fluids subjected to a light pattern with a checkerboard motif and different intensity levels. Thus, instead of completely switching off the light in the dark region, we dim its intensity so that the self-propulsion velocity in the dark region v_1 is such that $0 < v_1/v_2 < 1$, where v_1 is the self-propulsion velocity in the dark region and v_2 is the self-propulsion velocity in the bright region.

In Fig. 7(a), we can see the progression of an experimental run over time. A DMD was used to create the pattern seen on the initially uniform distribution. By 100 s, we can already see the emergence of structure, and a steady state is reached as time passes. To calculate number densities, we divide the number of swimmers

in a region by the total number of swimmers in the field of view, represented as N. Fig. 7(b) shows the number densities in each reservoir (ρ_1 and ρ_2) over time. The flux of particles across the barrier from the brighter to dimmer regions is initially greater, but it gradually levels off as the system reaches a steady state around 150 s, where the number densities remain constant. Even though the relative densities in each region remain constant, the snapshots taken at 150 s and 250 s are not equivalent, as particles are still traveling within their region and crossing the barrier into the neighboring region. In the experiment, we varied the contrast, and thus the v_1/v_2 ratio, and repeated it multiple times. In each experimental realization, the size of a box L_0 in the checkerboard pattern is significantly larger ($L_0 > 10 \times L_p$) than the persistence length of the light-activated swimmer L_p to best mimic an infinite reservoir. Fig. 7(c) shows the ratio of steady-state densities as a function of the inverse ratio of average speeds in each region. Each point on the plot represents one experimental observation that has reached a steady state. The data points agree with the equation $\rho_1/\rho_2 = v_2/v_1$, shown as a dashed line on the graph. When $v_2/v_1 = 1$, the activity is constant in space, and the number density profile is uniform in a steady state as well. However, this is only true when the ρ is relatively small, and particles rarely interact phoretically or via self-trapping. As $v_2/v_1 \to 0$, the disparity in the average speed characteristic of each reservoir becomes the highest, resulting in the spatial density profile in the steady state, having the highest contrast as well, with $\rho_1/\rho_2 \to 0$.

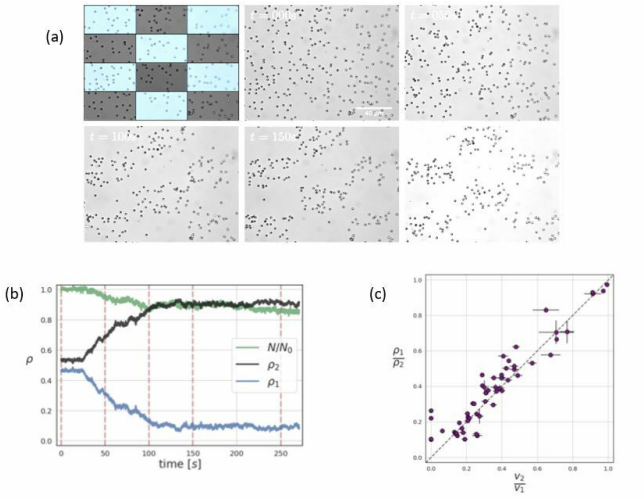

Fig. 7 Experimental results on smart templated assembly via a light pattern with a checkerboard motif. (a) Checkerboard light pattern and microscope images showing the evolution of the system at selected times. The organization of particles into a checkerboard structure develops with time. (b) Variation of the number density in the dark squares (ρ_2), in the bright square (ρ_1), and of the N/N_0 ratio with time, where N corresponds to the total numbers of microswimmers in view and N_0 to the total number of microswimmers in the system. (c) Plot of the ρ_1/ρ_2 density ratio against the v_2/v_1 velocity ratio.

In our simulations, we replicate the effect of a light pattern with a checkerboard motif by creating square regions with varying self-propulsion velocities. The darker regions have a velocity of $v_2 = s(\mathbf{r}) \times v_1$, where $0 < s(\mathbf{r}) < 1$, while the brighter regions have a velocity of $v_1 = 10^{-2}$. We simulate systems of 10^4 particles with a low packing fraction of $\phi = 0.05$ and use a checkerboard motif of 4×4 (16 square regions with characteristic length $L_0 = L/4$). This motif corresponds to a light pattern ten times larger than the persistence length in line with the experimental setup. Fig. 8 shows snapshots of the system at different times when using a velocity ratio of 0.2 and a 4×4 checkerboard. The simulation begins with a uniform spatial distribution of particles, but as time progresses, the particles accumulate in the dark regions and move away from the bright regions, resulting in a spatial distribution that closely matches the checkerboard motif of the light pattern (see also Movie 4 in the Supplementary Information).

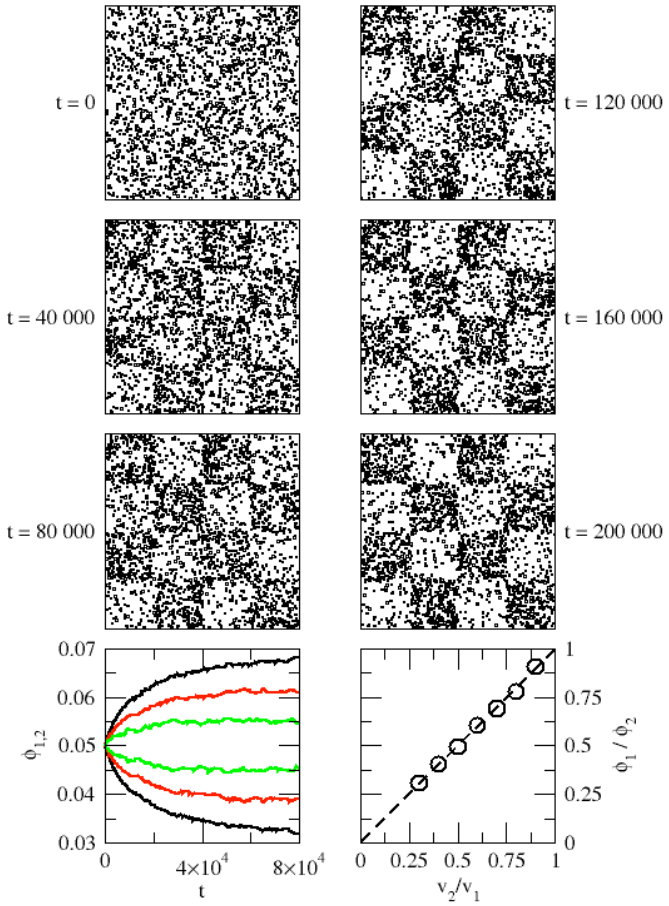

Fig. 8 Simulation results on smart templated assembly via a light pattern with a checkerboard motif. (Top) Snapshots of the system ($v_0 = 1$ and $\phi = 0.05$) showing the evolution at selected times for a 4×4 checkerboard motif. (Bottom left) Variation of the overall packing fraction in the dark squares (ϕ_2 - top branch in the plot) and bright squares (ϕ_1 - bottom branch in the plot) for different v_2/v_1 ratios with a 4×4 checkerboard motif (black line: $v_2/v_1 = 0.4$, red line: $v_2/v_1 = 0.6$, and green line: $v_2/v_1 = 0.8$) (Bottom right) Plot of ϕ_1/ϕ_2 against v_2/v_1 together with a linear fit (dashed line).

We carried out multiple simulations with varying velocity ratios across the $0 < v_2/v_1 < 1$ range. Our findings, displayed in Fig. 8, showcase the changes in packing fractions ϕ_1 and ϕ_2 in the dark and bright regions over time for specific velocity ratios. The results align with our earlier experiments on light patterns featuring individual bright or dark squares. The packing fraction

in the bright regions decreases exponentially with time, while the packing fraction in the dark regions increases accordingly. This behavior is also in agreement with the experiments (see Fig. 7). Upon comparing the results obtained for different velocity ratios, we find that the asymptotic behavior for the packing fractions, along with the ϕ_1/ϕ_2 ratios, varies based on the velocity ratio. For example, the asymptotic value for the packing fraction in the bright regions increases with the velocity ratio, while the asymptotic packing fraction in the dark regions decreases as the velocity ratio increases. Finally, our observations on the dependence of ϕ_1/ϕ_2 against v_2/v_1 in Fig. 8 indicate a linear dependence, in agreement with the experimental results reported in Fig. 7. More specifically, both the experimental data and the simulation results show that $\phi_1/\phi_2 = v_2/v_1$ over a wide range of $v_2 : v_1$ ratios. They are also consistent with the expectation that, for a broad range of active particles[26,29,39–41], the local packing fraction should be inversely proportional to the local self-propulsion velocity. This linear dependence holds for non-interacting random walkers[39], run-and-tumble particles, as evidenced in theoretical studies[40,41], and experimental work on *E.coli* bacteria[29], and recent research on active Brownian particles[26]. Our findings demonstrate that this same equation is valid for light-activated self-propelled colloidal particles or active Brownian particles with arbitrarily complicated light patterns. Additionally, our results provide a method for performing smart templated assembly using a specific light pattern, as well as controlling and regulating the local packing fraction by adjusting the local light intensity.

4 Conclusions

In this work, we carried out simulations on a simple active fluid composed of active Brownian particles and performed experiments on light-activated self-propelled particles to characterize templated assembly processes. We examined how light patterns can lead to inverse assembly, creating void regions within the fluid, or promote assembly, shaping clusters of particles that precisely adopt the shape of the pattern. Our focus was on proposing scaling relations that determine the characteristic time for assembly. The ratio of the size of the pattern (L_0) over the persistence length of the fluid (L_p) determines the characteristic time for inverse assembly. For assembly, the ratio is more complex ($L_0/(L_p\phi^{0.5})$), where ϕ is the packing fraction of the active fluid. The results obtained for the inverse assembly process are in agreement with experimental findings previously obtained on light-powered *E.coli* suspensions, while the scaling relation for this assembly process provides new information on this non-equilibrium process. We then explored the dynamics for the formation of larger clusters via light patterns that occur in a two-step process, with particles initially thrust into the dark regions before undergoing a diffusive motion toward the center of the dark pattern. We combined inverse assembly and assembly processes to template complex structures in the active fluid, achieving precise control of the local packing fraction throughout the fluid by modulating the light intensity in the dark and bright regions and, thus, the relative velocities in the two regions. The ability to fine-tune the packing fraction for the assembly goes beyond the capability of other assembly strategies that rely on thermodynamics to dictate the packing fraction of the assembly. This, in turn, paves the way for novel nonequilibrium assembly strategies for active matter by programming a high-resolution spatio-temporal pattern for the stimulus. Coating the particles with UV-sensitive cross-linkers would also enable fixing the designed material permanently for removal and external use.

Conflicts of interest

There are no conflicts to declare.

Acknowledgements

This material is based upon work supported by the U.S. Department of Energy, Office of Science, Office of Basic Energy Sciences under Award Number DE-SC0023673. This research used resources of the National Energy Research Scientific Computing Center, a DOE Office of Science User Facility supported by the Office of Science of the U.S. Department of Energy under Contract No. DE-AC02-05CH11231 using NERSC award BES-ERCAP0024334

Notes and references

1 M. C. Marchetti, J.-F. Joanny, S. Ramaswamy, T. B. Liverpool, J. Prost, M. Rao and R. A. Simha, *Rev. Mod. Phys.*, 2013, **85**, 1143.
2 J. Palacci, S. Sacanna, A. P. Steinberg, D. J. Pine and P. M. Chaikin, *Science*, 2013, **339**, 936–940.
3 A. Zöttl and H. Stark, *J. Phys. Condens. Matter*, 2016, **28**, 253001.
4 R. E. Isele-Holder, J. Elgeti and G. Gompper, *Soft Matter*, 2015, **11**, 7181–7190.
5 F. Caballero, C. Nardini and M. E. Cates, *J. Stat. Mech. Theory Exp.*, 2018, **2018**, 123208.
6 N. de Macedo Biniossek, H. Löwen, T. Voigtmann and F. Smallenburg, *J. Phys. Condens. Matter*, 2018, **30**, 074001.
7 J.-B. Delfau, C. López and E. Hernández-García, *New J. Phys.*, 2017, **19**, 095001.
8 S. Ramananarivo, E. Ducrot and J. Palacci, *Nat. Commun.*, 2019, **10**, 1–8.
9 P. S. Mahapatra and S. Mathew, *Phys. Rev. E*, 2019, **99**, 012609.
10 R. Ni, M. A. C. Stuart and M. Dijkstra, *Nat. Commun.*, 2013, **4**, 1–7.
11 S. Tarama, S. U. Egelhaaf and H. Löwen, *Phys. Rev. E*, 2019, **100**, 022609.
12 M. Han, M. Fruchart, C. Scheibner, S. Vaikuntanathan, J. J. De Pablo and V. Vitelli, *Nat. Phys.*, 2021, **17**, 1260–1269.
13 I. Essafri, B. Ghosh, C. Desgranges and J. Delhommelle, *Phys. Fluids*, 2022, **34**, 071301.
14 B. Trefz, S. K. Das, S. A. Egorov, P. Virnau and K. Binder, *J. Chem. Phys.*, 2016, **144**, 144902.
15 M. N. van der Linden, L. C. Alexander, D. G. Aarts and O. Dauchot, *Phys. Rev. Lett.*, 2019, **123**, 098001.
16 E. Mani and H. Löwen, *Phys. Rev. E*, 2015, **92**, 032301.
17 S. R. McCandlish, A. Baskaran and M. F. Hagan, *Soft Matter*,

2012, **8**, 2527–2534.
18 J. Stenhammar, R. Wittkowski, D. Marenduzzo and M. E. Cates, *Phys. Rev. Lett.*, 2015, **114**, 018301.
19 E. Tjhung, C. Nardini and M. E. Cates, *Phys. Rev. X*, 2018, **8**, 031080.
20 C. Tung, J. Harder, C. Valeriani and A. Cacciuto, *Soft Matter*, 2016, **12**, 555–561.
21 S. A. Mallory, C. Valeriani and A. Cacciuto, *Annu. Rev. Phys. Chem.*, 2018, **69**, 59–79.
22 S. K. Nandi and N. S. Gov, *Soft Matter*, 2017, **13**, 7609–7616.
23 P. Dolai, A. Simha and S. Mishra, *Soft Matter*, 2018, **14**, 6137–6145.
24 M. E. Cates, *Rep. Prog. Phys.*, 2012, **75**, 042601.
25 M. E. Cates and J. Tailleur, *EPL*, 2013, **101**, 20010.
26 J. Stenhammar, R. Wittkowski, D. Marenduzzo and M. E. Cates, *Sci. Adv.*, 2016, **2**, e1501850.
27 C. Lozano, B. Ten Hagen, H. Löwen and C. Bechinger, *Nat. Commun.*, 2016, **7**, 1–10.
28 J. Arlt, V. A. Martinez, A. Dawson, T. Pilizota and W. C. Poon, *Nat. Commun.*, 2018, **9**, 1–7.
29 J. Arlt, V. A. Martinez, A. Dawson, T. Pilizota and W. C. Poon, *Nat. Commun.*, 2019, **10**, 1–7.
30 G. Frangipane, D. Dell'Arciprete, S. Petracchini, C. Maggi, F. Saglimbeni, S. Bianchi, G. Vizsnyiczai, M. L. Bernardini and R. Di Leonardo, *Elife*, 2018, **7**, e36608.
31 O. Béja, L. Aravind, E. V. Koonin, M. T. Suzuki, A. Hadd, L. P. Nguyen, S. B. Jovanovich, C. M. Gates, R. A. Feldman, J. L. Spudich *et al.*, *Science*, 2000, **289**, 1902–1906.
32 J. M. Walter, D. Greenfield, C. Bustamante and J. Liphardt, *Proc. Natl. Acad. Sci.*, 2007, **104**, 2408–2412.
33 Y. Fily and M. C. Marchetti, *Phys. Rev. Lett.*, 2012, **108**, 235702.
34 Y. Fily, S. Henkes and M. C. Marchetti, *Soft Matter*, 2014, **10**, 2132–2140.
35 J. Palacci, S. Sacanna, S.-H. Kim, G.-R. Yi, D. J. Pine and P. M. Chaikin, *Philos. Trans. Royal Soc. A*, 2014, **372**, 20130372.
36 M. C. Marchetti, Y. Fily, S. Henkes, A. Patch and D. Yllanes, *Curr. Opin. Colloid Interface Sci.*, 2016, **21**, 34–43.
37 G. S. Redner, M. F. Hagan and A. Baskaran, *Phys. Rev. Lett.*, 2013, **110**, 055701.
38 M. P. Allen and D. J. Tildesley, *Computer simulation of liquids*, Oxford University Press, 1987.
39 M. J. Schnitzer, *Phys. Rev. E*, 1993, **48**, 2553.
40 J. Tailleur and M. Cates, *Phys. Rev. Lett.*, 2008, **100**, 218103.
41 J. Tailleur and M. Cates, *Europhys. Lett.*, 2009, **86**, 60002.